

Interfacial Localization and Voltage-Tunable Arrays of Charged Nanoparticles

Mrinal K. Bera,[†] Henry Chan,[‡] Daniel F. Moyano,[§] Hao Yu,[†] Sabina Tatur,[†] Daniel Amoanu,^{||} Wei Bu,[†] Vincent M. Rotello,[§] Mati Meron,[⊥] Petr Král,^{*,†,‡} Binhua Lin,^{*,⊥} and Mark L. Schlossman^{*,†}

[†]Department of Physics, University of Illinois at Chicago, Chicago, Illinois 60607, United States

[‡]Department of Chemistry, University of Illinois at Chicago, Chicago, Illinois 60607, United States

[§]Department of Chemistry, University of Massachusetts, Amherst, Massachusetts 01003, United States

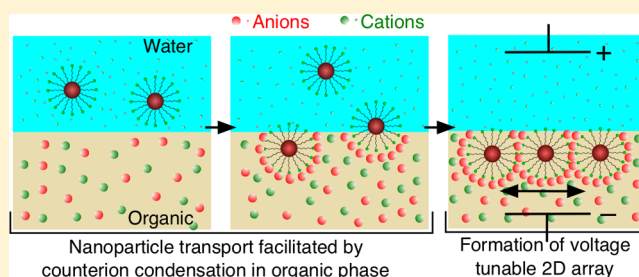
^{||}Department of Chemical Engineering, University of Illinois at Chicago, Chicago, Illinois 60607, United States

[⊥]Center for Advanced Radiation Sources, University of Chicago, Chicago, Illinois 60439, United States

Supporting Information

ABSTRACT: Experiments and computer simulations provide a new perspective that strong correlations of counterions with charged nanoparticles can influence the localization of nanoparticles at liquid–liquid interfaces and support the formation of voltage-tunable nanoparticle arrays. We show that ion condensation onto charged nanoparticles facilitates their transport from the aqueous-side of an interface between two immiscible electrolyte solutions to the organic-side, but contiguous to the interface. Counterion condensation onto the highly charged nanoparticles overcomes the electrostatic barrier presented by the low permittivity organic material, thus providing a mechanism to transport charged nanoparticles into organic phases with implications for the distribution of nanoparticles throughout the environment and within living organisms. After transport, the nanoparticles assemble into a two-dimensional (2D) nearly close-packed array on the organic side of the interface. Voltage-tunable counterion-mediated interactions between the nanoparticles are used to control the lattice spacing of the 2D array. Tunable nanoparticle arrays self-assembled at liquid interfaces are applicable to the development of electro-variable optical devices and active elements that control the physical and chemical properties of liquid interfaces on the nanoscale.

KEYWORDS: nanoparticles, liquid–liquid interface, transport, voltage-tunable array, ion condensation, charge-reversal



Multicharged nanoparticles (NPs), including proteins, viruses, and synthetic constructs, interact strongly with counterions in electrolyte solutions.¹ Electrostatic interactions produce spatial correlations between charged NPs and counterions, which are responsible for the condensation of DNA and proteins,^{2,3} as well as for charge reversal in aqueous colloidal dispersions.^{4,5} Counterion condensation onto micrometer-sized colloidal particles in aqueous dispersions is enhanced in the presence of highly charged counterions, typically trivalent or greater, whose stronger electrostatic interactions lead to stronger particle–counterion correlations.⁵ Although ion condensation is not expected to occur with monovalent counterions in aqueous solutions, recent experiments have demonstrated that condensation of monovalent counterions takes place on the organic side of an interface between aqueous and organic electrolyte solutions as a result of the stronger electrostatic interactions present in a low permittivity organic liquid.⁶

Here, experiments show that charged NPs dissolved in an aqueous phase can be transported from the aqueous to the organic side of an interface between two electrolyte solutions. Our classical molecular dynamics (MD) simulations show that

the transport of NPs is accompanied by counterion condensation onto the portion of the charged NPs exposed to the organic phase, which shields the NP charge from the low permittivity phase. The experiments also show that NPs form a nearly close-packed 2D array on the organic side of the interface, whose spacing can be tuned by varying the voltage. The tunability occurs because the voltage alters the interfacial distribution of supporting electrolytes, which mediate the interactions between NPs. The MD simulations also reveal that sharing of condensed counterions contributes to the coupling between neighboring NPs.

Location of Nanoparticles within the Interface. In our experiments, NPs consisting of a 2 nm gold core coated with ~100 positively charged trimethylammonium-terminated ligands⁷ (TTMA AuNP, Figure 1b) were injected into an aqueous electrolyte solution in contact with an organic electrolyte solution filling an electrochemical cell (Figure 1a,c and Supporting Information Section S1). Interfacial tension

Received: June 30, 2014

Revised: November 14, 2014

Published: November 17, 2014

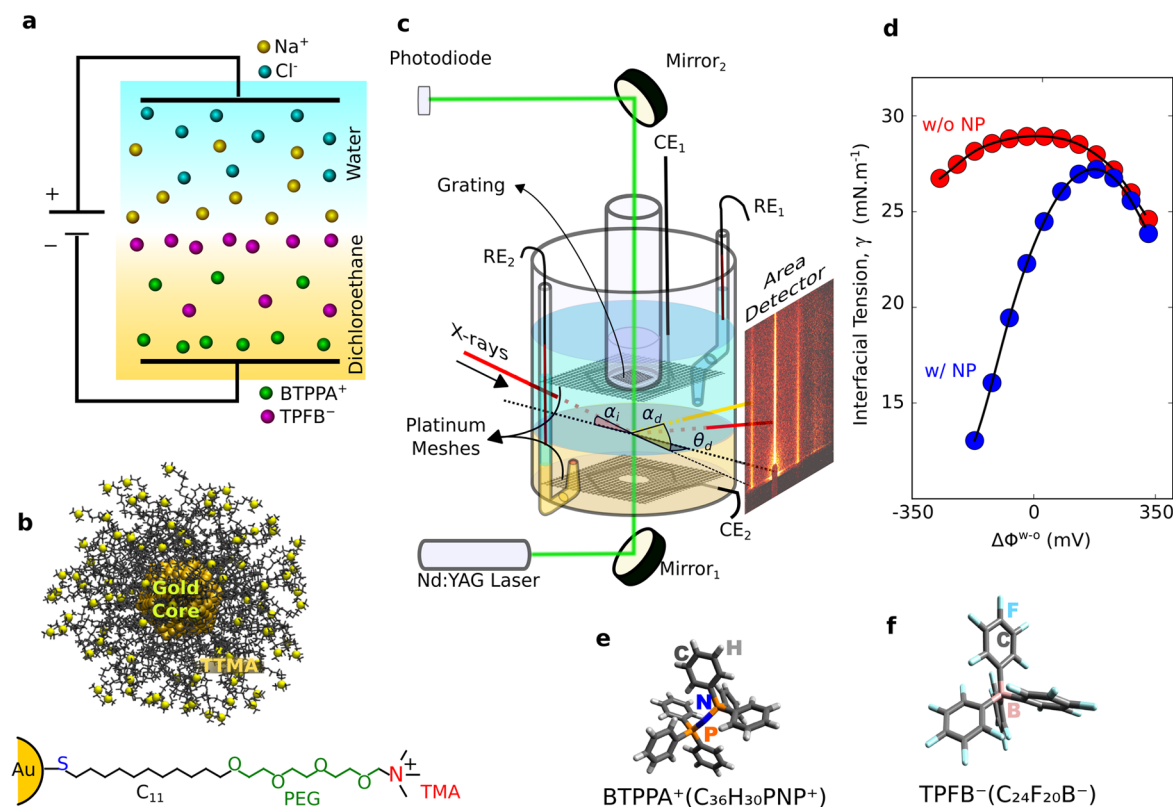


Figure 1. Sample and interfacial tension measurements. (a) Cartoon of ion distribution near a liquid–liquid interface between two immiscible electrolyte solutions when an electric potential difference $\Delta\phi^{w-o} > 0$ exists between the bulk phases, but without NPs. The supporting electrolytes are NaCl (5 mM) in water and BTPPA⁺ TPFB⁻ (5 mM, 54% dissociated) in 1,2-dichloroethane (DCE). (b) Gold NPs (2 nm core diameter) coated with ~ 100 TTMA ligands; ligand structure shown separately.⁷ (c) Electrochemical sample cell and experimental geometry for X-ray surface scattering measurements and quasi-elastic light scattering interfacial tension measurements (CE₁ and CE₂, counter electrodes made of Pt mesh; RE₁ and RE₂, reference electrodes are Ag wires coated with AgCl). (d) Interfacial tension measurements of the aqueous–organic interface as a function of electric potential difference $\Delta\phi^{w-o}$ with NPs (blue) and without NPs (red). Error bars (± 0.1 mN/m) are much smaller than the symbols. (e–f) Molecular structure of the organic ions BTPPA⁺ and TPFB⁻.

measurements indicate that NPs remain in the bulk aqueous phase as long as the electric potential difference $\Delta\phi^{w-o} = \phi(w) - \phi(o)$ between the aqueous (*w*) and organic (*o*) solutions remains negative. External control of $\Delta\phi^{w-o}$ to be slightly positive (e.g., 30 mV) leads to a reduction in interfacial tension due to the adsorption of TTMA AuNP onto the aqueous–organic interface, as expected from earlier predictions and observations of voltage induced adsorption of NPs.^{8,9} Subsequent tuning of $\Delta\phi^{w-o}$ in both positive and negative directions produces the reversible variation in interfacial tension illustrated by the blue curve in Figure 1d observed when NPs are present at the interface.

Accompanying the change in $\Delta\phi^{w-o}$ is a repositioning of the aqueous and organic supporting electrolytes (NaCl and bis(triphenyl phosphoranylidene) ammonium tetrakis pentafluorophenyl borate, BTPPATPFB, Figure 1e,f) from either bulk phase to the interface, or vice versa. For example, in the absence of NPs a positive $\Delta\phi^{w-o}$ produces an enhancement of Na⁺ on the water side of the interface and TPFB⁻ on the organic side of the interface (Figure 1a).¹⁰ Although values of $\Delta\phi^{w-o} \approx 0.1$ V lead to large electric fields on the order of 10⁸ V/m near the interface, the supporting electrolytes are not transported across the interface because they are essentially insoluble in the opposite phase over the experimental range of $\Delta\phi^{w-o}$.⁶

Interfacial tension measurements suggest that after injection into water, and equilibration at $\Delta\phi^{w-o} = 30$ mV, TTMA gold

NPs are transported to the interface but are located on its organic side. X-ray reflectivity measurements, discussed next, prove this conjecture. Measurements of interfacial tension γ in the electrochemical sample cell shown in Figure 1c are used to determine the interfacial excess charge per area Q_{tot} given by $Q_{\text{tot}} = -(\partial\gamma/\partial\Delta\phi^{w-o})_{T,p,\mu_i}$ (temperature *T*, pressure *p*, and chemical potential μ_i of species *i*).¹⁰ The excess charge Q_{tot} characterizes the enhancement of ions and NPs on the water side of the interface, whereas $-Q_{\text{tot}}$ characterizes the enhancement on the organic side. In the absence of NPs, the variation of interfacial tension with $\Delta\phi^{w-o}$, shown in Figure 1d, is characteristic of literature results.¹⁰ The presence of NPs produces a larger positive slope $\partial\gamma/\partial\Delta\phi^{w-o}$ at lower potentials (Figure 1d). This indicates a net enhancement of positive charge on the organic side of the interface, consistent with the transport of NPs to the organic side of the interface.

X-ray reflectivity measurements confirm the surprising result that water-soluble, heavily charged NPs are assembled into an interfacial monolayer located on the organic side of the interface. This experimental technique provides a direct probe of the NP location because it determines the variation in electron density perpendicular to the interface, that is, the electron density profile, with subnanometer resolution.¹¹ Reflectivity data shown in Figure 2a were measured with 30 keV X-rays at the ChemMatCARS beamline of the Advanced Photon Source and fit to a model of the interfacial electron

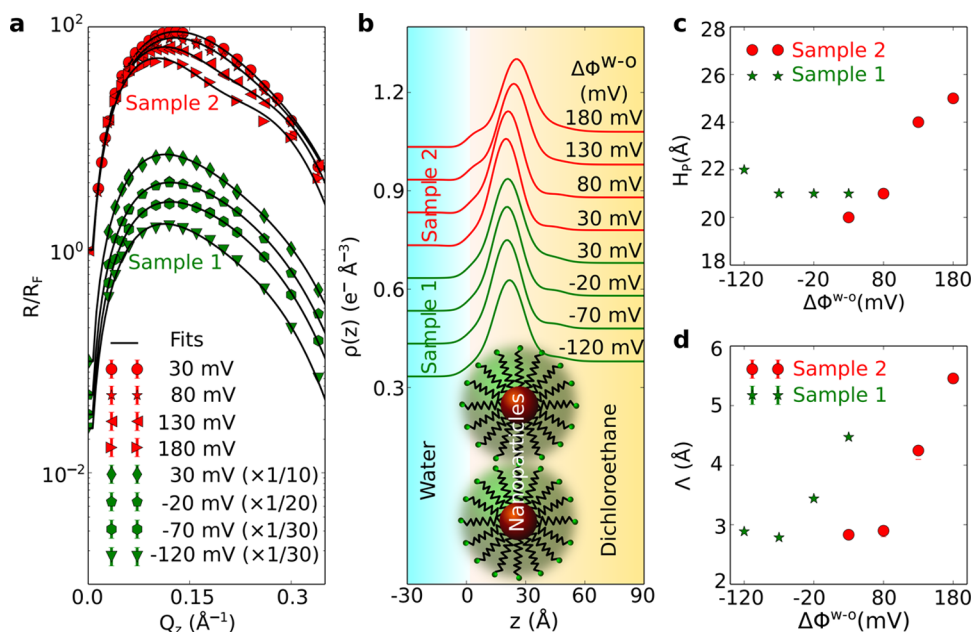


Figure 2. X-ray reflectivity measurements. The data shown are from samples that were initially equilibrated at $\Delta\phi^{w-o} = 30$ mV, then $\Delta\phi^{w-o}$ was increased (Sample 2) or decreased (Sample 1) from 30 mV. Cycling $\Delta\phi^{w-o}$ back and forth reproduces the interfacial structure with small variations in interfacial coverage and height distribution (Supporting Information Figure S7). (a) X-ray reflectivity R , normalized to the Fresnel reflectivity R_F from an ideal interface for TTMA gold NPs at the electrified water–DCE interface as a function of wave vector transfer normal to the interface, Q_z , for different electric potential differences $\Delta\phi^{w-o}$. Solid lines represent best fits to the model discussed in the text. (b) Variation of electron density $\rho(z)$ along the direction z (perpendicular to the interface) obtained from the fits in (a). A cartoon of NPs at the interface is shown. (c) The depth H_p of the NPs is given by the location of the peak maximum in (b). (d) The exponential decay length Λ of the depth distribution obtained from fitting X-ray reflectivity data. The discontinuity in Λ at $\Delta\phi^{w-o} = 30$ mV is the result of slight differences in equilibrated structure observed for different samples. Error bars are smaller than the symbols for panels a, c, and d.

density profile to determine the interfacial depth of the NPs and their depth distribution. A 2 nm spherical gold core, as measured by TEM (Supporting Information Figure S1), enclosed by a 1.8 nm ligand shell models the NPs. Variations of NP depth within the monolayer and NP polydispersity were then modeled by an exponential variation with decay length Λ . Further details of the interfacial electron density model and fitting to the X-ray reflectivity data are provided in the Supporting Information (Figures S2 and S3, Tables S1 and S2, and accompanying text).

Peaks in the electron density profiles in Figure 2b, which represent NP gold cores, show that NPs are located almost entirely on the organic DCE side of the interface and form a well-defined monolayer. The interfacial depth of the NP monolayer shows little change for negative potentials, but a small increase into the DCE phase as $\Delta\phi^{w-o}$ approaches +180 mV (Figure 2c). The small increase in peak width observed in Figure 2b as $\Delta\phi^{w-o}$ increases is characterized by an increase in decay length Λ of the depth distribution shown in Figure 2d.

Over this range of potentials, $-120 \text{ mV} \leq \Delta\phi^{w-o} \leq 180 \text{ mV}$, some NP ligands in the monolayer appear to remain in contact with the aqueous phase, though the NPs are immersed primarily in the DCE phase (Figure 2b). However, the interfacial tension at even higher potentials, up to 350 mV, approaches that of the pure interface without NPs (Figure 1d). Although this is consistent with the observed increase in penetration of NPs into the DCE phase as $\Delta\phi^{w-o}$ approaches 180 mV, additional X-ray measurements are required to determine whether or not NPs leave the organic side of the interface for $\Delta\phi^{w-o} > 180$ mV.

Self-Assembly of Voltage-Tunable Arrays. Figure 3a illustrates grazing-incidence small-angle X-ray scattering

(GISAXS) that reveals the 2D ordering of the interfacial monolayer of NPs.¹¹ The variation of Bragg rod intensity with Q_z (out-of-plane) is fit by a monolayer-thick 2D-array of NPs (whose analysis is shown in Supporting Information Figure S6), which is consistent with the results from our X-ray reflectivity studies. The 2D array at $\Delta\phi^{w-o} = 30$ mV is hexagonal, as determined by the presence of two symmetric first order $([1,0]/[0,1])$ Bragg rods at in-plane scattering wave vector $Q_{xy} = Q_{[10]} \approx \pm 0.114 \text{ \AA}^{-1}$ and faint second and third order Bragg rods at $Q_{xy} = Q_{[11]} \approx -0.197 \text{ \AA}^{-1}$ and $Q_{xy} = Q_{[20]} \approx -0.228 \text{ \AA}^{-1}$. Intensities of the GISAXS patterns integrated over Q_z , shown in Figure 3b, demonstrate that the lattice remains hexagonal for all measured potentials but variations in peak position and shape reveal voltage-dependent changes in lattice spacing and in-plane correlation length. The narrowest peaks are obtained after initial equilibration of the samples at $\Delta\phi^{w-o} = 30$ mV. The peak width determines the in-plane correlation length ξ , which measures the spatial extent of in-plane lattice order, to be 15 times the nearest-neighbor separation a for $\Delta\phi^{w-o} = 30$ mV. The larger widths of the peaks in Figure 3b at either larger or smaller $\Delta\phi^{w-o}$ indicate a decrease in ξ (Supporting Information Figure S5), which may be due to the creation of defects as the lattice expands or contracts.

Figure 3c illustrates a nearly linear increase of in-plane nearest-neighbor spacing, a , as $\Delta\phi^{w-o}$ is increased. This increase is not due to a loss of NPs from the interface, as demonstrated by an analysis of the percentage C of interface covered by NP unit cells ($C \approx 75\%$, Supporting Information Table S2), showing that the number of NPs on the interface is nearly constant as $\Delta\phi^{w-o}$ varies from -120 to 180 mV (Supporting Information Figure S4). Instead, the lattice spacing of the 2D NP array varies because $\Delta\phi^{w-o}$ determines the

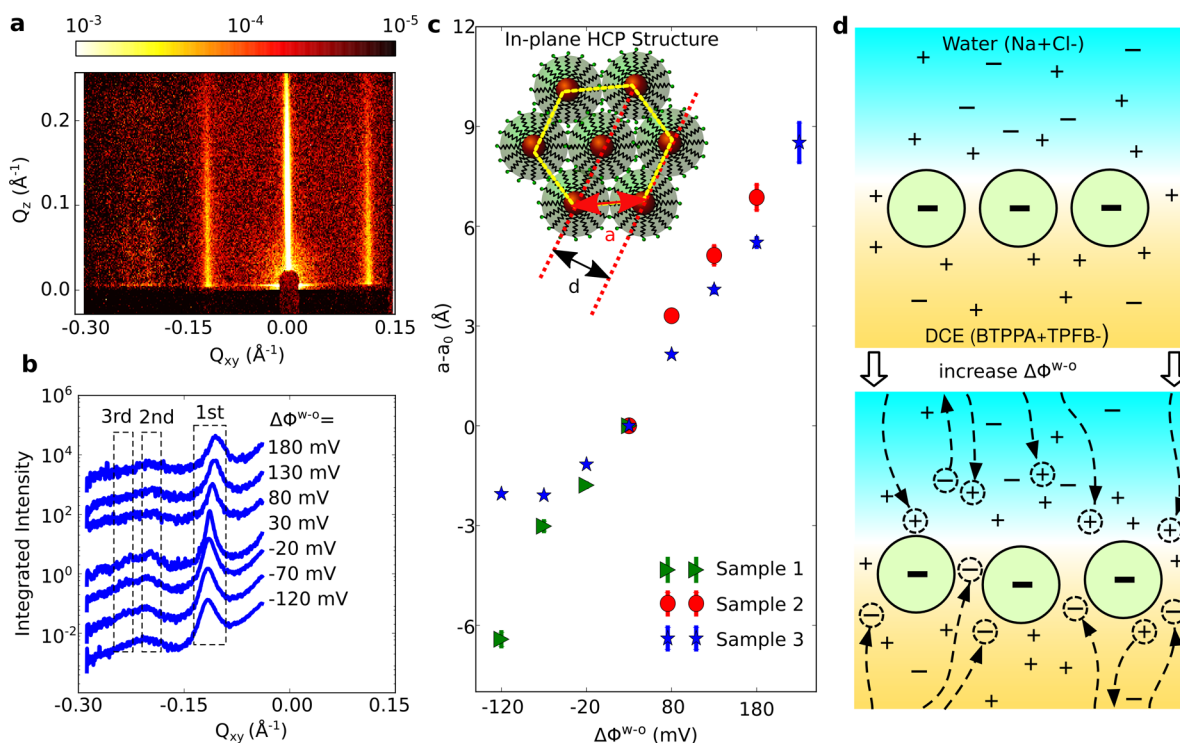


Figure 3. GISAXS measurements. (a) Bragg rods measured by grazing-incidence small angle scattering (GISAXS) from a 2D array of charged NPs at the electrified water–DCE interface for $\Delta\phi^{w-o} = 30$ mV, where Q_z is the wave vector transfer in the direction out of the plane of the interface and Q_{xy} is in the plane. (b) Intensity integrated over Q_z from 0 \AA^{-1} to 0.1 \AA^{-1} plotted as a function of Q_{xy} for different values of $\Delta\phi^{w-o}$ (measured from Sample 3). Each curve shows the equivalent of 2D grazing incidence diffraction with three diffraction peaks indicated. (c) Change in the nearest-neighbor spacing $a = 2d / \sqrt{3} = 4\pi / (\sqrt{3} Q_{[10]})$ for three different samples as a function of $\Delta\phi^{w-o}$ referenced to the spacing a_0 measured at $\Delta\phi^{w-o} = 30$ mV of the same sample ($a_0 = 67.2, 61.5,$ and 64.5 \AA for samples 1, 2, and 3, respectively). Inset: Cartoon of the 2D hexagonal close-packed structure of NPs with nearest-neighbor spacing a and lattice spacing d . (d) As explained in the text, NPs indicated by a “–” sign are charge-reversed with a net negative charge. TPFB[–] anions that condense on the NPs to reverse their charge are not shown separately. As $\Delta\phi^{w-o}$ increases, the net charge of the supporting electrolytes becomes more positive near the interface on the aqueous side and more negative on the organic side as a result of the re-distribution (indicated by arrows) of supporting electrolytes between bulk and interfacial regions.

concentration of electrolytes in the electrical double layers on either side of the interface and these electrolytes, in turn, modulate electrostatic interactions between NPs. In particular, increasing $\Delta\phi^{w-o}$, starting from either positive or negative values of $\Delta\phi^{w-o}$, makes the electrolyte environment on the organic side of the interface, that is, near the NPs, more negative (Figure 3d). If the total charge of each NP (including the TPFB[–] anions condensed on its surface) is positive, then a more negative electrolyte environment will reduce electrostatic repulsive forces between NPs, thereby reducing the lattice spacing. However, this contradicts the observations. Therefore, we need to assume that the total NP charge is not positive. This alternative scenario is illustrated in Figure 3d, which shows a monolayer of negatively charged NPs whose lattice spacing will increase with increasing $\Delta\phi^{w-o}$, as observed experimentally. Although the bare charge on each NP is +100, ion condensation of TPFB[–] counterions could reverse their net charge, as has been observed for larger colloids.⁵ Charge reversal, also known as overcharging, occurs when the bare charge of a particle is overcompensated by the condensation onto its surface of oppositely charged counterions whose net charge exceeds that of the original charge.⁵ Our MD simulations discussed later provide strong evidence for charge reversal of the NPs. This heuristic explanation of the trend in lattice spacing with $\Delta\phi^{w-o}$ relies upon the NPs’ effective charge remaining negative throughout the entire range of $\Delta\phi^{w-o}$, as described further in the Discussion.

The enhanced repulsion at larger $\Delta\phi^{w-o}$ should also increase the out-of-plane distribution of NPs, an expectation that is confirmed by the increase in decay length shown in Figure 2d. Note that the presence of NPs with negative effective charge does not contradict the results of interfacial tension discussed earlier, which probe the total excess charge of one (or the other) side of the interface. In that case, transport of a +100 bare-charged NP contributes +100 charges to the excess charge on the organic side of the interface whether or not organic counterions condense onto the NP and reverse its net charge.

Ion Condensation onto Submerging Nanoparticles.

Our MD simulations illustrate the transport of a single TTMA gold NP through the interface between an aqueous electrolyte solution and an organic (DCE) electrolyte solution (Figure 4a–d). The simulation was performed inside a $20 \times 20 \times 47 \text{ nm}^3$ unit cell (Figure 4e), initially filled with 100 Na⁺ and 150 Cl[–] in the aqueous phase and 100 BTPPA⁺ and 150 TPFB[–] in the organic phase. Global charge neutrality was satisfied by the +100 charges on the NP. This initial configuration included equal total charge of co-ions plus counterions in each bulk phase to simulate the experimental conditions of small $\Delta\phi^{w-o}$ at which NPs were measured on the organic side of the interface. In addition, there are more counterions (150) in each phase than charges on the bare NP (100) to allow for the possibility of charge reversal in either phase. Figure 4f shows the time dependence of the NP height, measured from the center of the gold core to the water–DCE interface, and the

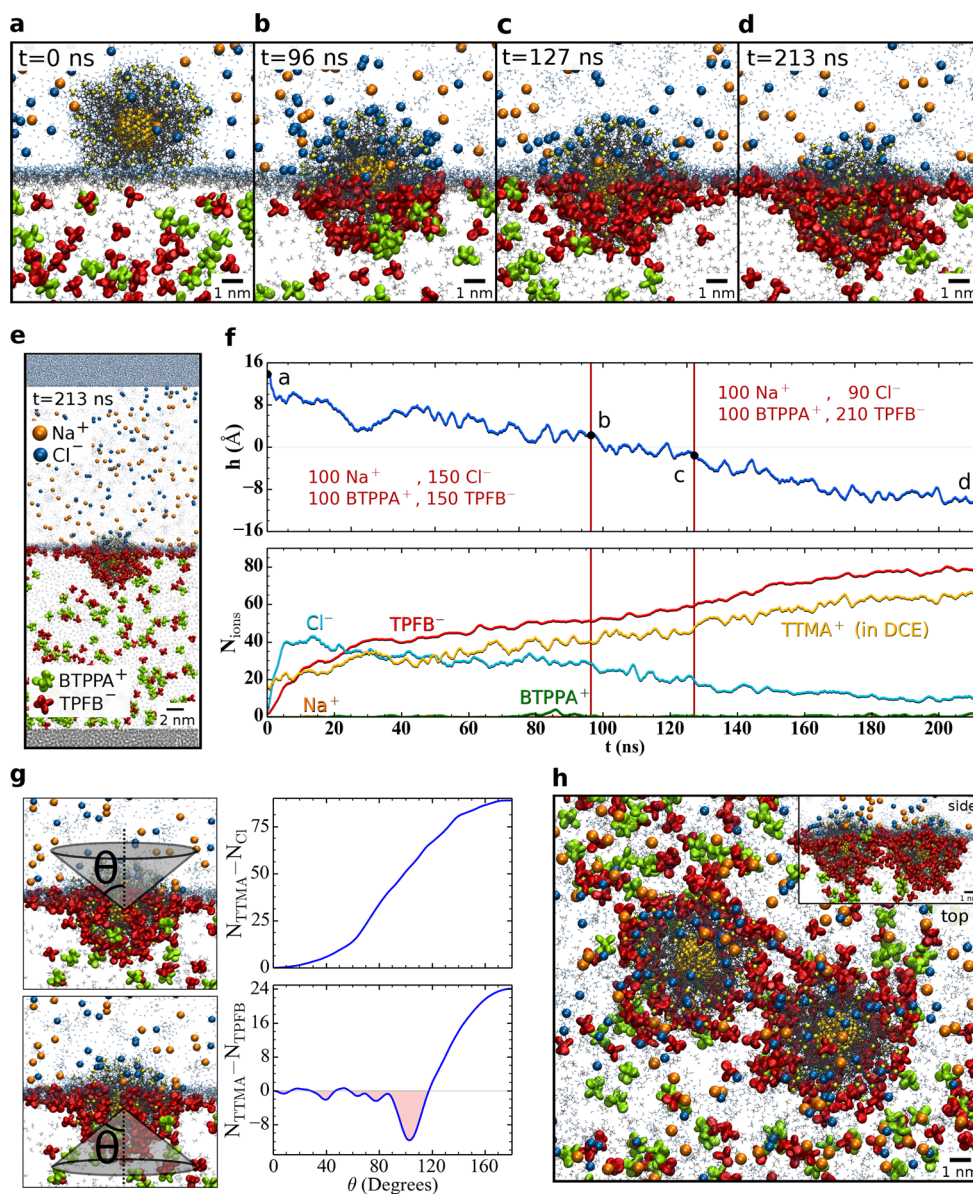


Figure 4. MD simulations. (a–d) Time sequence snapshots taken from a 213 ns MD simulation show the submersion of a NP from an aqueous (top) to an organic (bottom) electrolyte phase accompanied by the exchange of loosely bound Cl^- ions (blue) in the aqueous phase for condensed organic TPFB^- ions (red) in the organic phase. (e) Simulation cell (snapshot at 213 ns). Most solvent molecules are not shown for clarity. Two spatially fixed solvent layers are shown in gray at the top and bottom (see Supporting Information Section S6). (f) Time dependence of the NP submersion height, h , measured from the center of the Au core to the interface, and the number of ions, N_{ions} , within 1 nm of the NP surface. The vertical lines at $t = 96$ ns and $t = 127$ ns indicate when the number of Cl^- and TPFB^- ions in the bulk phases are adjusted (see text). (g) Time-averaged analysis of the last 40 ns MD simulation trajectory for the charge summed over NP surface cations (TTMA^+) plus either Cl^- (top) or TPFB^- (bottom) that are within 1 nm of the NP surface and within the specified cone angle. The cone apex is located at the center of the Au core. The minimum at $\sim 105^\circ$ in the lower panel contains TPFB^- ions within the ring of three-phase contact line between NP and aqueous and organic phases. The pink fill shows that the portion of the NP exposed to the organic phase is charge reversed. (h) Two NPs in the simulation cell in (e) form a stable pair at $t = 68$ ns (top view with inset of side view).

number of ions within 1 nm of the NP surface. An initial quick partial submersion of the particle is accompanied by adsorption of TPFB^- ions that replace Cl^- . Counterion adsorption onto the NP eventually alters the ion balance in our simulation cell, by releasing Cl^- into the aqueous phase and removing TPFB^- from the organic phase. This produces a potential difference that opposes further submersion. To reset the ion balance, 30 Cl^- ions are removed from the aqueous phase and 30 TPFB^- ions added to the DCE phase at ~ 96 ns and again at ~ 127 ns. Counterion condensation of TPFB^- onto the NP is observed as it crosses the interface (Figure 4a–d).

Figure 4f shows that the number of TPFB^- counterions within 1 nm of the NP surface is larger by ~ 13 ions than the number of TTMA^+ ligands exposed to the DCE phase by the end of the simulation. Many of these excess charges are located in the denser region of TPFB^- ions along the “ring” of three-phase contact line between NP and aqueous and organic phases. Excluding the excess charges in this ring, the remaining part of the NP exposed to the organic phase is slightly charge reversed (Figure 4g). The bottom right panel of Figure 4g shows that the net charge is approximately -2 for cone angles between 70° and 90° that account for most of the NP

submerged into the organic phase, but excluding the three-phase contact ring. Likewise, an MD simulation of an isolated TTMA Au NP placed within a DCE electrolyte solution exhibits a small overcharging of -2 (Supporting Information Figure S8). Stacking of TPFB⁻ rings, as observed in the simulation in Figure S8, allow TPFB⁻ ions to pack more closely on the NP surface, potentially contributing to the efficiency of charge reversal. Charge reversal of the NP is consistent with our explanation of lattice expansion with increasing $\Delta\phi^{w-o}$ (Figure 3c). As expected for monovalent ions in water, the upper panels of Figure 4g show that Cl⁻ ions are not condensed onto the water-side of the NP and that side is not charge reversed. The simulation results provide evidence that NPs are transported from the polar aqueous side of the interface to the organic side as a result of their stronger affinity to bind TPFB⁻ ions than Cl⁻ ions.

Two-NP systems were also simulated to study the interactions between NPs at the interface (Figure 4h). The simulations were performed under the same conditions and in the same cell used for the single NP simulations. The simulation was prepared by adding 1 NP plus the nearest 30 Cl⁻ and 70 TPFB⁻ ions, as extracted from the single NP simulation, to the final equilibrated configuration of the single NP system. Ions that were initially positioned between the NPs were repositioned to the solution under them. The interparticle distance between the NPs stabilized at ~ 7.4 nm within 50 ns (Supporting Information Figure S9) and TPFB⁻ ions from the solution migrated to the region between the NPs.

Discussion. The strength of correlations between a charged NP and a counterion, which can be measured by the ratio of electrostatic interaction energy to thermal energy, varies inversely with the permittivity of the solvent.¹ Sufficiently strong electrostatic interactions, such as those present in the low permittivity organic DCE phase ($\epsilon_{r,DCE} = 10.43$), have been previously shown to produce condensation of TPFB⁻ monovalent ions on the water–DCE interface without NPs.⁶ The low permittivity of DCE can also produce ion condensation of TPFB⁻ ions onto NPs and, subsequently, reverse their effective charge. Other effects, such as preferential chemical interactions between TPFB⁻ ions and the NP, could contribute to the ion condensation.

Our simulations of a single NP show that ion condensation occurs in the bulk organic phase in the absence of an applied electric field (Supporting Information Figure S8). Related to this, our experiments show that NPs are transported to the organic side of the interface under the action of a small applied potential equal to 30 mV. Simulations with equal numbers of counterions on either side of the interface, which model a small $\Delta\phi^{w-o}$, confirm that a NP is spontaneously transported across the interface with ion condensation occurring on the organic side, as well as charge reversal of the portion of the NP exposed to the organic phase. Ion condensation provides a driving force to move TTMA gold NPs from the aqueous to the organic DCE phase.

These observations lead to our understanding that NPs are charge reversed due to ion condensation that occurs as a result of their presence in the low permittivity organic phase, not as a result of an applied electric field. Figure 3d describes our suggestion that the voltage-tunability of the 2D array of NPs is the result of voltage-induced variations in the density of counterions in the vicinity of charge-reversed NPs. To summarize, ion condensation on NPs and their charge reversal occur when NPs are exposed to the organic phase, even at very

low voltage, whereas voltage-tunability is due to counterion-mediated interactions between the charge-reversed NPs. The separation of these two effects arises because the electrostatic energies associated with the potential range of the experiment are much smaller than the electrostatic energy of attraction between a condensed counterion and its NP.

To address the existence of a 2D lattice of NPs, we simulated two NPs, shown in Figure 4h. The MD simulation results indicate that the two NPs stabilize within close proximity to each other, where they appear to share a few TPFB⁻ ions in the condensed layer of counterions. Atomistic simulations of larger interfacial NP lattices tunable by voltages would necessitate significantly larger computational resources than we have at our disposal. Monte Carlo simulations of the liquid–liquid interface between immiscible electrolyte solutions may also provide an accessible computational scheme to study this lattice.¹² Although analytic theory has described voltage-tunable lattices at the liquid–liquid interface, the effects of ion condensation and charge reversal have not been previously considered in this context.⁸ Other theoretical works have discussed several correlation effects that could be important in stabilizing the observed lattice of charged NPs, including mechanisms to share multivalent counterions between neighboring surfaces or colloids,^{5,13} as observed in our two-NP simulation, as well as Coulomb-depletion¹⁴ forces that arise due to excluded volume effects. In this context, it should be noted that our experiments demonstrate that the 2D crystallization cannot be due to pure repulsion, as previously observed for charged micrometer-sized colloids at the liquid–liquid interface.¹⁵ Our X-ray reflectivity measurements show that NPs are present over only 75% of the interface and the two-NP simulations confirm that NPs can be stably bound while occupying only a fraction of the interface. If exclusively repulsive forces stabilized the lattice, NPs would spread apart from each other as far as possible within the confinement of the interface, thereby leading to larger lattice constants than those measured.

When condensation of organic counterions onto highly charged NPs takes place at an aqueous–organic interface, the charge of the NP is shielded as it is drawn across the interface into the low polarity organic environment. In combination with water-borne transport of NPs,¹⁶ this route into organic phases adds to the possible pathways along which charged NPs, both synthetic and natural, can be transported through complex heterogeneous environments consisting of aqueous and organic regions that exist within biological organisms and the natural environment. Our experiments also show that electrical control over interfacial transport leads to voltage-tunable self-assembly of NPs at the interface. Fine-tuning chemical and electrostatic interactions on both sides of the interface may ultimately lead to control over the location of charged NPs within the interfacial region, thereby providing new possibilities to control interactions with aqueous and organic components for purposes such as multiphase trace analyte detection.¹⁷ NP arrays self-assembled at liquid interfaces are applicable to the development of electrovariable optical devices,¹⁸ plasmonics,^{19,20} and active elements controlling molecular transport across liquid interfaces.

■ ASSOCIATED CONTENT

📄 Supporting Information

Materials, experimental methods and analysis, and MD simulations are discussed further in the Supporting Informa-

tion. This material is available free of charge via the Internet at <http://pubs.acs.org>.

AUTHOR INFORMATION

Corresponding Authors

*E-mail: schloss@uic.edu.

*E-mail: nayanbera@gmail.com or lin@cars.uchicago.edu.

*E-mail: pkral@uic.edu.

Notes

The authors declare no competing financial interest.

ACKNOWLEDGMENTS

We acknowledge support from the UIC CRB Pilot Grant program (to M.L.S.), NSF-DMR-1309765 and ACS-PRF-53062-ND6 (to P.K.), and CMMI-1025020 (to V.M.R.). ChemMatCARS is supported by NSF-CHE-1346572. The APS at Argonne National Laboratory is supported under DOE-BES Contract No. DE-AC02-06CH11357. The computations were partly performed on the NCSA and NERSC networks.

ABBREVIATIONS

BTPPATPFB, bis(triphenylphosphoranylidene) ammonium tetrakis(pentafluorophenyl)borate; DCE, 1,2-dichloroethane; MD, molecular dynamics; TTMA AuNP, trimethylammonium terminated ligands on gold nanoparticle

REFERENCES

- (1) Levin, Y. *Rep. Prog. Phys.* **2002**, *65*, 1577–1632.
- (2) Bloomfield, V. A. *Curr. Opin. Struct. Biol.* **1996**, *6*, 334–341.
- (3) Zhang, F.; Skoda, M. W. A.; Jacobs, R. M. J.; Zorn, S.; Martin, R. A.; Martin, C. M.; Clark, G. F.; Weggler, S.; Hildebrandt, A.; Kohlbacher, O.; Schreiber, F. *Phys. Rev. Lett.* **2008**, *101* (14), 148101–1 - 148101–4.
- (4) James, R. O.; Healy, T. W. *J. Colloid Interface Sci.* **1972**, *40*, 53–64.
- (5) Quesada-Perez, M.; Gonzalez-Tovar, E.; Martín-Molina, A.; Lozada-Cassou, M.; Hidalgo-Alvarez, R. *ChemPhysChem* **2003**, *4*, 234–248.
- (6) Laanait, N.; Mihaylov, M.; Hou, B.; Yu, H.; Vanysek, P.; Meron, M.; Lin, B.; Benjamin, I.; Schlossman, M. L. *Proc. Nat. Acad. Sci. U.S.A.* **2012**, *109*, 20326–20331.
- (7) Miranda, O. R.; Chen, H. T.; You, C. C.; Mortenson, D. E.; Yang, X. C.; Bunz, U. H. F.; Rotello, V. M. *J. Am. Chem. Soc.* **2010**, *132* (14), 5285–5289.
- (8) Flatte, M. E.; Kornyshev, A. A.; Urbakh, M. *J. Phys.: Condens. Matter* **2008**, *20* (7), 073102.
- (9) Su, B.; Abid, J. P.; Fermín, D. J.; Girault, H. H.; Hoffmannová, H.; Krtil, P.; Samec, Z. *J. Am. Chem. Soc.* **2004**, *126* (3), 915–9.
- (10) Samec, Z. *Pure Appl. Chem.* **2004**, *76* (12), 2147–2180.
- (11) Pershan, P. S.; Schlossman, M. L. *Liquid Surfaces and Interfaces: Synchrotron X-ray Methods*; Cambridge University Press: Cambridge, 2012.
- (12) Guerrero-García, G. I.; Jing, Y.; de la Cruz, M. O. *Soft Matter* **2013**, *9*, 6046–6052.
- (13) Zwanikken, J. W.; de la Cruz, M. O. *Phys. Rev. E* **2010**, *82* (5), 050401–1 - 050401–4.
- (14) Allahyarov, E.; D'Amico, I.; Löwen, H. *Phys. Rev. Lett.* **1998**, *81*, 1334–1337.
- (15) Leunissen, M. E.; Zwanikken, J.; Roij, R. v.; Chaikin, P. M.; Blaaderen, A. v. *Phys. Chem. Chem. Phys.* **2007**, *9*, 6405–6414.
- (16) Lowry, G. V.; Casman, E. A. Nanomaterial Transport, Transformation, and Fate in the Environment: A Risk-Based Perspective on Research Needs. In *Nanomaterials: Risks and Benefits in NATO Science for Peace and Security Series - C: Environmental Security*; Linkov, I., Steevens, J., Eds.; Springer: Dordrecht, The Netherlands, 2009.

(17) Cecchini, M. P.; Turek, V. A.; Paget, J.; Kornyshev, A. A.; Edel, J. B. *Nat. Mater.* **2013**, *12*, 165–171.

(18) Flatte, M. E.; Kornyshev, A. A.; Urbakh, M. *J. Phys. Chem. C* **2010**, *114*, 1735–1747.

(19) Kinnan, M. K.; Chumanov, G. *J. Phys. Chem. C* **2010**, *114*, 7496–7501.

(20) Turek, V. A.; Cecchini, M. P.; Paget, J.; Kucernak, A. R.; Kornyshev, A. A.; Edel, J. B. *ACS Nano* **2012**, *6*, 7789–7799.